

# *A Minutely Solar Irradiance Forecasting Method Based on Real-time Sky Image-Irradiance Mapping Model*

Fei Wang<sup>1,2,3</sup>, Zhiming Xuan<sup>1</sup>, Zhao Zhen<sup>1,4,\*</sup>, Yu Li<sup>5</sup>, Kangping Li<sup>1</sup>, Liqiang Zhao<sup>6,7</sup>, Miadreza Shafie-khah<sup>8</sup>, João P.S. Catalão<sup>9</sup>

1. Department of Electrical Engineering, North China Electric Power University, Baoding 071003, China

2. State Key Laboratory of Alternate Electrical Power System with Renewable Energy Sources (North China Electric Power University), Beijing 102206, China

3. Hebei Key Laboratory of Distributed Energy Storage and Micro-grid, North China Electric Power University, Baoding 071003, China

4. State Key Lab of Power System, Department of Electrical Engineering, Tsinghua University, Beijing 100084, China

5. Dispatch and Control Center, State Grid Xinjiang Electric Power Co., Ltd, Urumqi 830018, China

6. China Electric Power Research Institute, Beijing 100192, China

7. State Grid Energy Internet Research Institute, Beijing 100192, China

8. School of Technology and Innovations, University of Vaasa, 65200 Vaasa, Finland

9. Faculty of Engineering of University of Porto and INESC TEC, 4200-465 Porto, Portugal

\* Correspondence: zhenzhao@ncepu.edu.cn; Tel.: +86-13663399630

Received: date; Accepted: date; Published: date

**Abstract**—Accurate minutely solar irradiance forecasting is the basis of minute-level photovoltaic (PV) power forecasting. In this paper, a minutely solar irradiance forecasting method based on real-time surface irradiance mapping model is proposed, which is beneficial to achieve higher accuracy in solar power forecasting. First, we extract the red-green-blue (RGB) values and position information of pixels in sky images after background elimination and distortion rectification, to explore the mapping relationship between sky image and solar irradiance. Then a real-time sky image-irradiance mapping model is built, trained, and updated according to real-time sky images and solar irradiance. Finally, the future solar irradiance within the time horizons varying from 1 min to 10 min ahead are capable to be forecasted by using the latest updated surface irradiance mapping model with extracted input from the current sky image. The average measures of proposed method by using MAPE, RMSE, MBE are 22.66%, 92.72, -1.26% for blocky clouds; 20.44%, 132.15, -1.06% for thin clouds and 18.82%, 120.78, -0.98% for thick clouds, thus deliver much higher forecasting accuracy than other benchmarks.

**Keywords**—Solar irradiance forecasting; minutely; sky image; surface irradiance mapping; real-time model

## I. INTRODUCTION

### 1.1 Background and literature review

Solar photovoltaic (PV) power generation is one of the most promising renewable energy resources, which has developed rapidly and gained more and more worldwide attention in the past few decades [1]. According to the nature of electricity, the generation, transmission, distribution, and utilization of electric power are entirely based on real-time synchronization [2], which means PV power generation systems are accessed on both generation side and load side [3]. In the case of China, for generation side, large-scale grid-connected PV power plants are the dominant application form in its early development stage [4]; while for load side, the distributed PV such as building-integrated PV (BIPV) has also developed rapidly in recent years [5]. However, solar power is a kind of uncontrollable energy resource with high random fluctuations and uncertainties, which poses significant challenges to the power system operation [6]. In cloudy days, the solar irradiance received by PV modules could be highly random and fluctuant due to the motion of clouds [7], which will result in a minutely fast random fluctuation effect on solar PV power output [8]. Therefore, with the increasing penetration of PV power in the power grid, the characteristics of energy generation side and load side will both change significantly, thus lead to difficulties on maintaining the dynamic balance between supply and demand sides [9], which result in the possibilities of accident occurrence, such as voltage rise and vacillations, variation in frequency harmonics and other severe problems [10,11].

In order to avoid the occurrence of the above situations, various solutions have been proposed, including backup generators [12], battery reserves [13], demand response [14,15], power system scheduling, and dispatches [16], etc. However, there are still existing limitations in all these solutions. The power ascend/decline rate of backup generators is restricted by the unit ramp

1 rate, which may result in difficulties to meet the incremental power generation need [17]. As for battery reserves,  
2 massive-scale energy storage is still difficult to realize for the sake of production costs and storage capacity restrictions [18].  
3 Concerning the lack information on electricity consumption behavior of residential users, it's also hard to achieve demand  
4 response technologies [19]. Besides, the effectiveness of these mentioned solutions largely relies on the accuracy of  
5 forecasting with various time horizons, thus help the grid dispatching side to update and correct day-ahead scheduling [20].  
6 Accurate forecasting can not only provide future PV power output data for grid operators, thus to mitigate the adverse effect of  
7 random PV power on the power grid [21], but also bring data support for demand response and prolong the service life of  
8 reserve battery by reducing times of charge and discharge [22].

9 In recent years, PV power forecasting technologies have been widely studied, developed, and improved. In this area, early  
10 researches were mainly based on the data-driven algorithm and statistical analysis theory [23]. According to the historical  
11 power output and meteorological data, researchers can excavate the mapping relationship between the historical impact factor  
12 data and future power generation output [24]. However, this type of researches is limited to external numerical variation law of  
13 historical PV power output and impact factor data record, thus become difficult to forecast the fast fluctuation of PV power  
14 with a high time resolution. Hence, to explore the core physical reasons behind the power changes, the fundamental factors  
15 that causing the sudden change of irradiance and PV power are necessary to be explored [25]. In other words, the prediction of  
16 cloud motion is an essential part of ultra-short-term irradiance forecasts [26]. Based on the above considerations, solar  
17 irradiance or PV power forecasting methods using sky images are presented, which shows better potential and accuracy than  
18 traditional forecasting methods based on historical data and statistical learning models [27].

19 In general, forecasting methods should be selected according to the forecasting temporal-spatial and horizon scale. As for  
20 medium and long-term forecasting horizon, in [28], a Particle Swarm Optimization (PSO) optimized extreme learning  
21 machine (ELM) method was applied to forecast medium and long-term solar PV power output with different time intervals: 15  
22 min, 30 min, 60 min, and showed better performance compared with other basic machine learning methods. However,  
23 compared with longer term forecasts, short-term and ultra-short-term forecasts are getting more attention from researchers.  
24 For short-term forecasting, literature [29] proposed a backpropagation neural network (BPNN) model to forecast day-ahead  
25 PV outputs. The aerosol index was an input, as the researchers claimed it was strongly (linearly) correlated with the attenuation  
26 of incident solar radiation. In [30], a hybrid approach for day-ahead power output forecasting of a PV installation was  
27 developed by integrating generalized regression neural network (GRNN) with a couple of feed-forward neural network  
28 (FFNN) and multiple linear regression (MLR). Stepwise regression was employed for selecting the most strongly correlated  
29 meteorological parameters as input for this model. For these types of forecasts of which the forecast horizon is only one day or  
30 a few days ahead, meteorology impact factors extraction based numerical weather prediction (NWP) and satellite images have  
31 been widely mentioned in various literature [31–33]. Despite abundant meteorology information contained in NWP and  
32 images captured by satellite imagery systems, these types of techniques have still been limited in practical application because  
33 the local information cannot be depicted quite elaborately [34]. Here we mainly focus on local and shorter term forecasts  
34 (lower than one hour) where artificial intelligence methods are generally applied. Therefore, sky image-based methods are  
35 widely used for the sake of its higher temporal and spatial resolution in ultra-short-term forecasts, as cloud information can be  
36 seen as a crucial factor to the established training model [35]. The use of all-sky cameras is a promising solution for intra-hour  
37 forecast horizons as introduced in [36] and [37]. For ground-based sky imaging systems, one study applied cloud indices  
38 obtained from a total sky imager (TSI) and extracted by cloud classification algorithms [38]. The cloud indices derived from  
39 infrared radiometric (IR) measurements to report improved global horizontal irradiance (GHI) results for 1-h forecasting by  
40 using artificial neural network (ANN) models. More recently, literature [39] used images obtained from TSI to produce  
41 prediction of GHI single-point solar irradiance sensors located at the University of California San Diego. Their study also  
42 offers a method to calculate cloud field velocity by computing matching errors of the future image and current images. The  
43 results suggest that TSI can be deemed as a good manner for extracting the cloud field velocity message, to achieve the  
44 forecasting horizons of up to 15–20 min. A more deterministic approach which consists in researching the position and the  
45 motion direction of the clouds so that to calculate the consuming time when the cloud covers the sun [40]. Apart from cloud  
46 detection and motion information, sky images contain more information impacting the GHI prediction: especially the cloud  
47 cover and the type of clouds. This kind of information can be combined with machine learning methods to compute the  
48 forecast.

## 49 *1.2 Motivation and contribution*

50 Regional irradiance mapping for distributed roof-mounted PV power systems is capable to bring convenience to acquire  
51 real-time irradiance distribution information in a certain region. On the basis of this surface irradiance mapping,  
52 ultra-short-term irradiance forecast can be achieved within a few minutes ahead after cloud displacement vector (CDV)  
53 calculation. It enables to show benefits to prolong the service time of the storage battery and reduce the frequency of its quick

1 charge. What's more, minutely forecast is conducive to grid dispatching which can provide guidance and detailed correction.

2 However, most existing researches use the measured data from a single point sensor to predict irradiance, which means they  
3 can only predict the irradiance information at a fixed location in real time [41,42]. In other words, it can be elaborated that  
4 when a sky image is captured, usually there is a corresponding irradiance value tested by solar instrumentation, thus directly  
5 present a point-to-point peer relationship. Nevertheless, there is still less or even no relevant studies on presenting irradiance  
6 distribution in the local region based on real-time sky images, as well as minutely forecasting method based on this sky  
7 image-irradiance mapping model. Therefore, in this paper, a minutely irradiance forecasting method based on real-time sky  
8 image-irradiance mapping model is proposed to fill this gap.

9 The novel method initially preprocesses raw captured sky images with background elimination and distortion rectification,  
10 then the red-green-blue (RGB) values and position information (distance from the pixel to the sun center) of sky image pixels  
11 are extracted as model input. During the process of characteristic extraction, only the center of cloud region part which will  
12 cover the sun in the next few minutes are considered to be desired image pixels. For each sky image, 10 cloud region parts that  
13 cause blocked-sun effect can be distinguished after CDV calculation. Then set these sky pixels' RGB values and position  
14 information as input, while corresponding irradiance values as output to train the mapping model by using BPNN and support  
15 vector machine (SVM) respectively. The establishment can be finished for the sky image-irradiance mapping model. Based on  
16 cloud-base height data, after importing each pixel's information in a real-time sky image, the mapping figure which depicts  
17 surface irradiance distribution in a local region can be generated. Finally, we can apply this model to achieve minutely  
18 irradiance forecast within the time horizon from 1 min to 10 min. Each forecasting by this model needs to be updated with new  
19 sample data before the current time. The simulation results show the better performance of the proposed minutely irradiance  
20 forecasting method compared with the other two benchmarks.

21 The main contributions of this paper are summarized as follows:

- 22 (1) The mapping relationship from the spatial distribution of cloud to the temporal distribution of irradiance is constructed  
23 utilizing cloud motion calculation. That is to build a model with cloud position and RGB values information as input  
24 and the corresponding irradiance as output.
- 25 (2) A real-time modeling method is proposed for the sky image-irradiance mapping model. Based on the latest observed sky  
26 images, the color features of a specific cloud at different distances from the sun are extracted to update the training data, so  
27 that the trained model can adapt to the current cloud conditions.
- 28 (3) A minutely solar irradiance forecasting method based on real-time sky image-irradiance mapping model is proposed,  
29 which can improve the accuracy of minutely solar irradiance forecasting.
- 30 (4) Actual data is applied to evaluate the effectiveness of the proposed method in various cloud conditions and weather  
31 environments.

## 32 II. METHODOLOGY

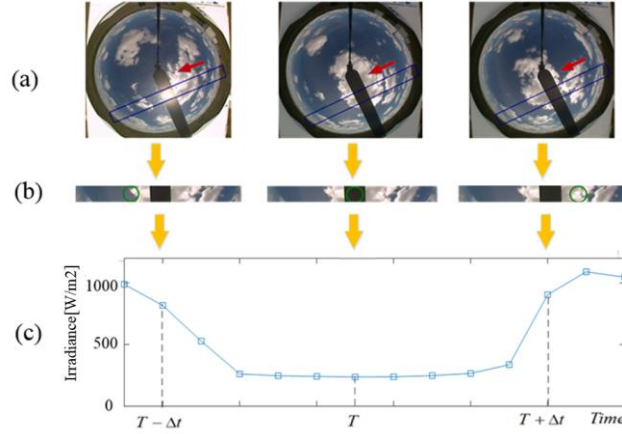
### 33 2.1 Sky image-irradiance mapping relationship

34 It is well known that aerosols, water vapor, cloudiness are the most critical meteorological factors which have an impact on  
35 the amount of solar irradiance reaching the ground surface. Among these, PV power is subject to cloud generation, dissipation,  
36 deformation, and motion, which may cause severe fluctuation and intermittency on power output. Out of various  
37 cloud-tracking methods in existence, ground-based sky imaging systems are recently getting a remarkable momentum applied  
38 to irradiance forecasting. Compared with satellite-based forecasts, sky images-based forecasts can distinctly describe local sky  
39 information, such as sun-block situations and cloud distribution at a high-resolution level. Therefore, sky image is becoming  
40 the optimum choice to acquire cloud information in minute level ultra-short-term irradiance prediction.

41 When the sun rays penetrate the atmospheric layer, blue sky and white clouds can be formed by the interaction between  
42 radiation and atmospheric molecules. However, when clouds are too thick for sun rays to pass through, clouds will turn to dark  
43 gray. In the presented joint photographic experts group (JPEG) sky image, RGB model is generally composed by R (red), G  
44 (green), B (blue) values, with the range of each pixel's channel value from 0 to 255, thus generate different colors by setting  
45 various RGB values. Referring to RGB table, we enable to observe that the RGB values of blue sky, white cloud, and dark gray  
46 cloud are about (0, 0, 255), (255, 255, 255), (180, 180, 180) respectively.

47 Since the surface irradiance is mainly related to the shape and thickness of the cloud which near the sun, we can easily  
48 conclude that, the sky region near the sun with diverse RGB values (blue or white) will affect the amount of solar irradiance  
49 reaching at crystalline silicon cells, thus changing PV power output. In other words, when the sun is located in the blue sky

1 area, irradiance always keeps at a high level; when the sun is covered by white or gray cloud, irradiance will dropdown. Based  
 2 on this observation, the classification of cloud and blue sky pixels can be achieved by RGB values distinction. Besides, it also  
 3 means RGB information of pixels is closely related to irradiance value, which supplies a theoretical support for minute-level  
 4 sky image-irradiance mapping model establishment. The detailed illustration is exemplified in Fig. 1.



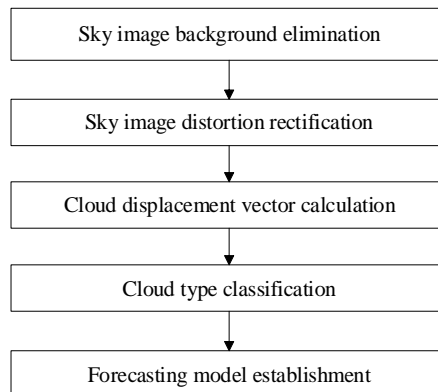
5  
 6 **Fig. 1.** Relationship between raw sky images and corresponding irradiance values. (a) 3 sky images with time interval  $\Delta t$  in each consecutive pair. (b) Circular  
 7 cloud regions which cover the sun. (c) Corresponding irradiance values at time  $T - \Delta t, T, T + \Delta t$ .

8 In Fig.1, 3 consecutive sky images selected with the same time interval  $\Delta t$  in each image pair are presented in Fig.1(a).  
 9 From artificial observation, the cloud is moving towards the bottom left direction. In this paper, we assume that cloud  
 10 motion is a smooth process, which means the speed of the cloud can not be changed violently during a short period. After  
 11 cloud motion displacement calculation of each image pair, cloud regions that cover the sun at time  $T - \Delta t, T, T + \Delta t$  can be  
 12 determined, marked by the green circle in the second sky image presented in Fig.1(b). Therefore, from one sky image (such  
 13 as the second image in Fig.1(a)), cloud region information which covers the sun at adjacent time can also be acquired. The  
 14 irradiance values at time  $T - \Delta t, T, T + \Delta t$  which corresponding to circled cloud regions are shown in Fig.1(c). It is easy to  
 15 infer that when the sun is located in the blue sky or white cloud region, the corresponding irradiance values are much higher  
 16 than the ones in the dark gray cloud environment. Thus, spatial information in sky images can be transformed as temporal  
 17 information of irradiance series, which denoted in (1).

18 
$$Irr(t \pm \Delta t_i) = \phi(F(x \pm \sum_{j=1}^i \Delta x_j, y \pm \sum_{j=1}^i \Delta y_j)) \quad i = 1, 2, \dots, n \quad (1)$$

19 Here  $Irr$  means irradiance;  $x, y$  mean the sun center;  $\Delta x_j, \Delta y_j$  represent the cloud motion displacement at the  $j$ th min;  
 20  $F$  means cloud feature in the circular region with radius  $R$  and point center  $(x \pm \sum_{j=1}^i \Delta x_j, y \pm \sum_{j=1}^i \Delta y_j)$ ;  $\phi$  is the mapping  
 21 relation.

22 In this way, depending on calculated cloud motion vectors, we can extract the information of the sky region which will  
 23 cover the sun in the next few minutes. After processing the model input with pixels' information and irradiance output, the  
 24 sky image-mapping model can be well established by utilizing machine learning methods. Based on this sky  
 25 image-irradiance mapping relation, future work on minutely irradiance forecasting can be achieved. Except for cloud feature  
 26 extraction, some other image and data pre-processing technology should be implemented in our work. Here we present a  
 27 brief flow chart (Fig. 2) to show the process of the proposed minutely irradiance forecasting method.



1 **Fig. 2.** A brief flow chart for the process of proposed minutely irradiance forecasting method.

2 **2.2 Sky image pre-processing**

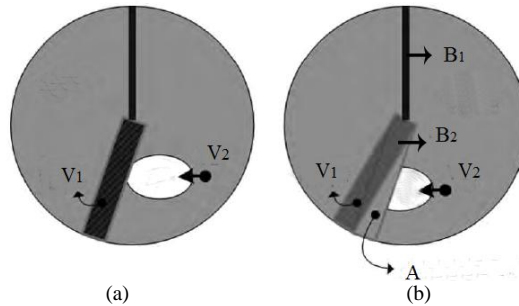
3 Ground observations using a sky imager provide a visual measurement of regional skydome over a central PV power plant,  
 4 thus deliver a sub-kilometer view of the cloud field. Due to its high temporal and spatial resolution, sky image-based  
 5 approaches are rapidly evolving in recent years. The TSI is mainly composed of a heated rotating hemispherical mirror with a  
 6 down-pointing charge-coupled device (CCD) camera located above it. To shoot the sky region as wide as possible, the mirror  
 7 is applicable for fish-eye lens in arc-shape. Therefore, before cloud characteristic extraction, necessary processing technique  
 8 is required to eliminate image distortion. Besides, to protect the mirror from damage, sun-tracking shadow-band is inserted  
 9 into the hemispherical mirror to insulate direct sunlight, which results in missing sky image information covered by the  
 10 shadow-band. To sum up, sky image background elimination and image distortion rectification are the key steps for image  
 11 data pre-processing.

12 **2.2.1 Sky image background elimination**

13 To acquire more sky information and remove the obstacles in cloud characteristic refining process, the sky information gap  
 14 due to camera arm and shadow-band coverage needs to be filled particularly [43]. Fig.3 shows a representation of the  
 15 background elimination and repair process. In this part, we first calculate the cloud motion displacement  $(x_0, y_0)$  between  
 16 two sky images  $I_1$  and  $I_2$ , in which image  $I_2$  is 5 min later than image  $I_1$ . Based on the assumption of smooth cloud  
 17 motion process, we can probably determine the motion speed of the cloud as  $V_2$  after cloud motion displacement calculation.  
 18 Due to the shadow-band is always following with the sun, to fill the black area of image  $I_1$ , covered partial region  $A$  can be  
 19 filled in part of image  $I_2$  based on calculated motion value  $(x_0, y_0)$ , which means sky information moves up  $x_0$  pixels, and  
 20 moves  $y_0$  pixels in right direction. The relationship between pixel information  $I(x_a, y_a)$  and  $I(x_b, y_b)$  in image  $I_1, I_2$   
 21 respectively is shown in (2):

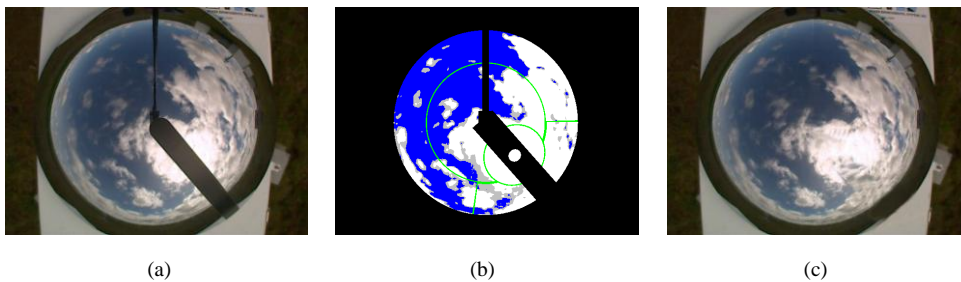
22 
$$I(x_a, y_a) = I(x_b + v_2 \cos \theta, y_b + v_2 \sin \theta) \quad (2)$$

23 Concerning other covered regions: camera arm part  $B_1$  and residual unfilled part  $B_2$ , here we apply bilinear interpolation  
 24 contraction algorithm to fill this gap.



27 **Fig. 3.** Sketch map of sky image background elimination. (a) Sky image  $I_1$  at some point. (b) Sky image  $I_2$  captured in 5 min later after image  $I_1$ .

28 In order to ascertain which part needs to be coped with, here we utilize the after-processing image generated by TSI data  
 29 acquisition software to classify blind regions. The black part in Fig.4(b) with zero-gray value in the circular region can be  
 30 distinguished as a filling area. The performance of sky image background elimination is presented as Fig.4.



32  
33  
34 **Fig. 4.** (a) Raw sky image. (b) Processed image by image processing system installed on a sky imager. (c) Sky image after background elimination.

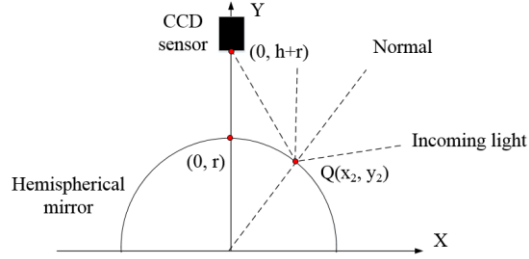
### 2.2.2 Sky image distortion rectification

For the sake of geometric distortion produced by the fisheye lens, the size and location of objects usually vary from the actual situation, resulting in low accuracy of detected cloud motion vectors. What's more, large amounts of information around the image boundary can be compressed which leads to information ambiguity. Therefore, in consideration of this impact on surface irradiance mapping model establishment, it is necessary to apply image distortion rectification to deal with this problem [44].

In Fig.5, light path mechanisms that demonstrate the imaging principle of a sky imager is presented. Assuming that pixel  $S(x_1, y_1)$  is formed by light reflection through the point  $Q(x_2, y_2)$  at the surface of hemispherical mirror, then the relationship between  $S(x_1, y_1)$  and  $Q(x_2, y_2)$  can be represented as (3)-(4):



(a)



(b)

Fig. 5. (a) Raw sky image. (b) Schematic diagram of light path mechanisms on sky imager.

$$x_2 = k\sqrt{x_1^2 + y_1^2} \quad (3)$$

$$y_2 = \sqrt{r^2 - x_2^2} \quad (4)$$

where  $k$  means conversion factor between pixel distance and actual distance,  $r$  means the radius of the hemispherical mirror. Then the zenith angle  $a$  of pixel  $S$  can be expressed as (5), azimuth angle  $b$  can be expressed as (6).

$$a = 2 \arcsin \frac{x_2}{r} + \arctan \frac{x_2}{h + r - \sqrt{r^2 - x_2^2}} \quad (5)$$

$$b = \arctan \frac{y_1}{x_1} \quad (6)$$

Therefore, the coordinates of the cloud pixel in local region  $(x, y)$  can be derived as:

$$x = h_c \times \tan a \times \sin b \quad (7)$$

$$y = h_c \times \tan a \times \cos b \quad (8)$$

Here  $h_c$  represents the cloud-base height of the main cloud cluster in a sky image, which can be obtained from thermal infrared cloud imager. On the basis of the formulas mentioned above, image distortion rectification can be achieved, thus transforming the original distorted view into a normal view. This pre-processing technique mitigates the deformation on sky images and further reduces inaccuracy level to irradiance forecasting.

### 2.3 Cloud displacement vector calculation

In order to determine the corresponding relationship between the specific area of sky image and the elements in the irradiance sequence, the calculation of cloud displacement vector (CDV) is essential to obtain the direction and distance of the cloud movement.

Considering the requirement of computing time and robustness for CDV calculation, here we apply an improved Fourier phase correlation (FPC) method based on affine transform which is corresponding to image-phase-shift-invariance (IPSI) property [45]. The CDV is also very important to the mapping modeling of surface irradiance [46], which would impact the load pattern clustering [47], the household characteristic identification [48, 49], and the aggregated capacity forecasting for load aggregators [50] with behind-meter distributed solar PV systems. In addition, the distributed active power regulator of islanded microgrids [51, 52], distributed cooperative control for microgrids [53-55] and PV-assisted EV charging stations [56] will be greatly influenced by the output power forecasting error of high penetration level distributed solar PV systems during the active power sharing and frequency control processes of microgrids.

1 FPC enables to acquire object's motion information, especially rigid parallel motion, by transforming image information  
 2 from the time domain into the frequency domain. After processed with Fourier transform, it is easy to find that displacement  
 3 information is saved in the phase spectrum, not amplitude spectrum, which brings convenience to motion calculation. The  
 4 detailed deduction of FPC method is given by (9)-(12).

5 We assume that the grayscale matrix resolution of an image  $f(x, y)$  is  $M \times N$ . Then after processed with discrete Fourier  
 6 transform (DFT), the transformed form  $F(u, v)$  is able to be denoted as follows:

$$7 \quad F(u, v) = \sum_{x=0}^{M-1} \sum_{y=0}^{N-1} f(x, y) e^{-j2\pi(\frac{ux}{M} + \frac{vy}{N})} = |F(u, v)| e^{-j\phi(u, v)} \quad (9)$$

$$(u = 0, 1, \dots, M-1; v = 0, 1, \dots, N-1)$$

8 where  $x, y$  and  $u, v$  represent the pixel's cartesian coordinates, Frequency domain coordinates, respectively.

9 If two sky images  $f_1(x, y)$  and  $f_2(x, y)$  merely differ with a displacement vector  $(x_0, y_0)$ , then the relation between  
 10  $f_1(x, y)$  and  $f_2(x, y)$  will be:

$$11 \quad f_2(x, y) = f_1(x - x_0, y - y_0) \quad (10)$$

12 In order to extract the information in phase spectrum, the cross-power spectrum (CPS) can be deduced as (11):

$$13 \quad C(u, v) = \frac{F_1(u, v) F_2^*(u, v)}{|F_1(u, v) F_2^*(u, v)|} = e^{j2\pi(\frac{ux_0}{M} + \frac{vy_0}{N})} \quad (11)$$

14  $F^*(u, v)$ ,  $|F(u, v)|$  mean complex conjugate and amplitude of  $F(u, v)$ , respectively. Then we process  $C(u, v)$  by inverse  
 15 discrete Fourier transform (IDFT), to acquire the motion displacement  $(x_0, y_0)$ , which is calculated as (12).

$$16 \quad F^{-1}\{C(u, v)\} = \delta(x - x_0, y - y_0) \quad (12)$$

17 However, for the sake of irregular shape change of cloud cluster, rigid motion is not always preserved. This case probably  
 18 generates a considerable amount of noise during image registration, which results in true displacement value  $(x_0, y_0)$   
 19 submerged by other noise pulses. Therefore, to solve this problem, we rotate the same sky image pair for multiple times with  
 20 various specific angle in a clockwise direction, then FPC calculation is proceeded. After rotated anticlockwise the same angle  
 21 for impulse matrix  $\delta(x - x_0, y - y_0)$ , plenty of calculation results can be generated.

22 To determine the desired final displacement, it is necessary to extract the most credible CDV from the result dataset, which  
 23 generated by improved FPC method mentioned above. Here we utilize centroid iteration to achieve final displacement vector  
 24 extraction.

25 Assume that the coordinates of CDVs for each rotation are:

$$26 \quad D = \{(x_1, y_1), (x_2, y_2), \dots, (x_n, y_n)\} \quad (13)$$

27 The average value of all the CDVs in dataset  $D$  can be calculated as:

$$29 \quad D_{ave} = (\frac{1}{n} \sum_{i=1}^n x_i, \frac{1}{n} \sum_{i=1}^n y_i) \quad (14)$$

30 Next, calculate the Euclidean distance between  $D_{ave}$  and each vector in dataset  $D$ , then select the farthest vector and remove  
 31 it from  $D$ . Following the step of new average  $D_{ave}'$  update by (14), the relative distance  $d$  between  $D_{ave}$  and  $D_{ave}'$  can be  
 32 depicted as (15).

$$33 \quad d = \frac{|D_{ave} - D_{ave}'|}{|D_{ave}|} \quad (15)$$

34 Here we set a threshold value  $\varepsilon$  to decide when to finish the iteration process. When  $d > \varepsilon$ , let  $D_{ave} = D_{ave}'$  and repeat the  
 35 steps mentioned above, or else stop the centroid iteration process and consider  $D_{ave}$  as the final displacement result. The  
 36 threshold  $\varepsilon$  has an impact on the number of iterations and concentration level of residual CDVs, which is usually determined

1 according to the image size and the distribution of dataset. The pseudo-code of centroid iteration process is listed as follows in  
2 Table 1.

3 **Table 1** The pseudo-code of centroid iteration process.

<b>Input:</b> Cloud displacement vector dataset $D = \{(x_1, y_1), (x_2, y_2), \dots, (x_n, y_n)\}$ . The threshold value $\varepsilon$ during centroid iteration process.
1: Calculate average value $D_{ave}$ of all the CDVs in $D$ ;
2: Calculate Euclidean distance between $D_{ave}$ and each vector in dataset $D$ , get distance set $D = \{D_1, D_2, D_3, \dots, D_n\}$ ;
3: Select the farthest vector $D_{max}$ , remove the corresponding displacement result from $D$ ;
4: Calculate relative distance $d$ by formula (15);
5: <b>while</b> $d > \varepsilon$ <b>do</b>
6: $D_{ave} = D_{ave}'$ ;
7:     Calculate new distance set $D$ ;
8:     Calculate relative distance $d$ ;
9: <b>end while</b>
<b>Output:</b> The final cloud displacement vector $D_{ave}$ .

4

#### 5 2.4 Cloud type classification

6 To verify the accuracy of irradiance forecasting method proposed in this paper, it is essential to classify various weather  
7 types. In order to simplify the identification process, processed images generated by TSI computational software  
8 preliminarily provides pixel classification for corresponding raw sky images. Based on TSI built-in cloud classification  
9 algorithm application, each pixel can be distinguished as sun, cloud, background type by different gray values in processed  
10 images. However, not all pixels are classified exactly in processed images, in a few cases, cloud pixels will in  
11 misidentification. Therefore, to reduce classification inaccuracy, here we develop our own method to conduct cloud type  
12 classification process.

13 As we know, different colors are composed of diverse RGB values. For sky image, it mainly consists of blue, white, gray  
14 colors, the RGB values of several major colors are depicted in Table 2.

15 **Table 2** RGB values of blue, white, and several shades of gray colors.

Color	R value	G value	B value
Blue	0	0	255
White	255	255	255
Dark gray	192	192	192
Gray	128	128	128
Dim gray	105	105	105

16

17 To distinguish the weather type of each image, firstly, it is necessary to know the pixel is a cloud or not. As shown in  
18 Table 2, the values are both consistent in each RGB channel except for blue color. Here we use red-blue-ratio (RBR) index  
19 presented in (17) to distinguish blue from other two colors, which can determine a pixel as clear sky or just a cloud.

$$20 \quad RBR = \frac{B - R}{B + R} \quad (17)$$

21 Due to the similarity between R value and G value for clouds with different colors, lightness index  $L$  is proposed to  
22 classify white and gray color. The formula is defined as follows:

$$23 \quad L = \frac{R + G + B}{3} \quad (18)$$

24 Here we set  $T_1$ ,  $T_2$  as the thresholds of RBR and  $L$ , to further identify a pixel into 3 categories: sky, thin cloud and  
25 thick cloud.



1

$$C = \begin{cases} \text{Sky} , & RBR > T_1 \\ \text{Thin cloud} , & RBR \leq T_1, L > T_2 \\ \text{Thick cloud} , & RBR \leq T_1, L \leq T_2 \end{cases} \quad (19)$$

2

3

4

Numerical values of  $T_1$  and  $T_2$  should be set reasonably, so as to avoid excessive discrepancies in classification results. In this paper, we set the thresholds  $T_1 = 0.07$ ,  $T_2 = 200$ . After cloud pixel classification, sky images can be divided into 4 weather types: clear sky, blocky cloud, thin cloud and thick cloud.

5

6

7

8

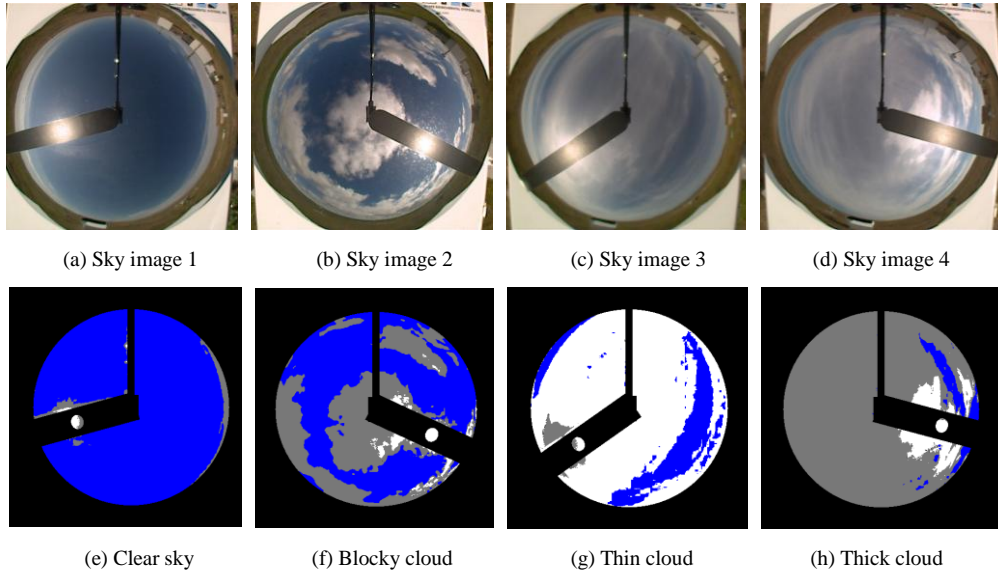
The objective function of weather type classification depicted in (20), consists of 3 terms: sky region proportion  $P_{sky}$ , thin cloud proportion  $P_{thin}$  and thick cloud proportion  $P_{thick}$ . According to (17)-(20), the final identification results for 4 weather types are presented in Fig.6. For Fig.6(e)-Fig.6(h), blue, white, gray colors are chosen to represent sky, thin cloud, thick cloud in pixel level respectively.

9

$$Classification = \begin{cases} P_{sky} \geq 90\% , & \text{Clear sky} \\ 30\% < P_{sky} < 90\% , & \text{Blocking cloud} \\ P_{sky} \leq 30\% \ \& \ \frac{P_{thin}}{1 - P_{sky}} \geq 50\% , & \text{Thin cloud} \\ P_{sky} \leq 30\% \ \& \ \frac{P_{thick}}{1 - P_{sky}} \geq 50\% , & \text{Thick cloud} \end{cases} \quad (20)$$

10

11



12

13

14

15

**Fig. 6.** Raw sky image and corresponding identification image in 4 weather types: (a)(e) in clear sky condition; (b)(f) in blocky cloud condition; (c)(g) in thin cloud condition; (d)(h) in thick cloud condition.

16

### 2.5 Influence of cloud type on sky image-irradiance mapping model

17

18

19

20

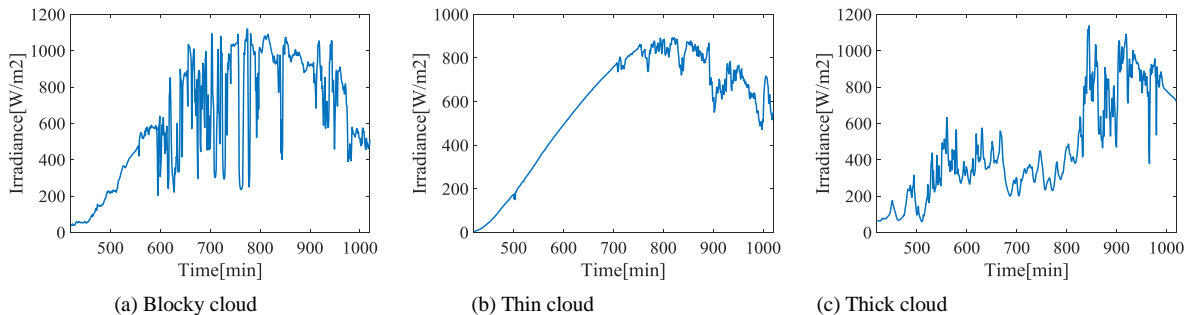
21

22

In order to verify the practical application effect of the proposed forecasting method in this work comprehensively, we select 3 cloud conditions based on different cloud shapes and thickness: blocky cloud, thin cloud, and thick cloud. Considering that only when the sun rises to the minimum solar zenith angle set advanced, then the sky imager starts to work and capture local sky field information. In this paper, datasets are gathered from 7:00 to 17:00. In Fig.7, irradiance curves of 3 cloud condition are presented, of which the data are selected on May 2, 2017 in blocky cloud, August 26, 2016 in thin cloud, and June 8, 2016 in thick cloud.

23

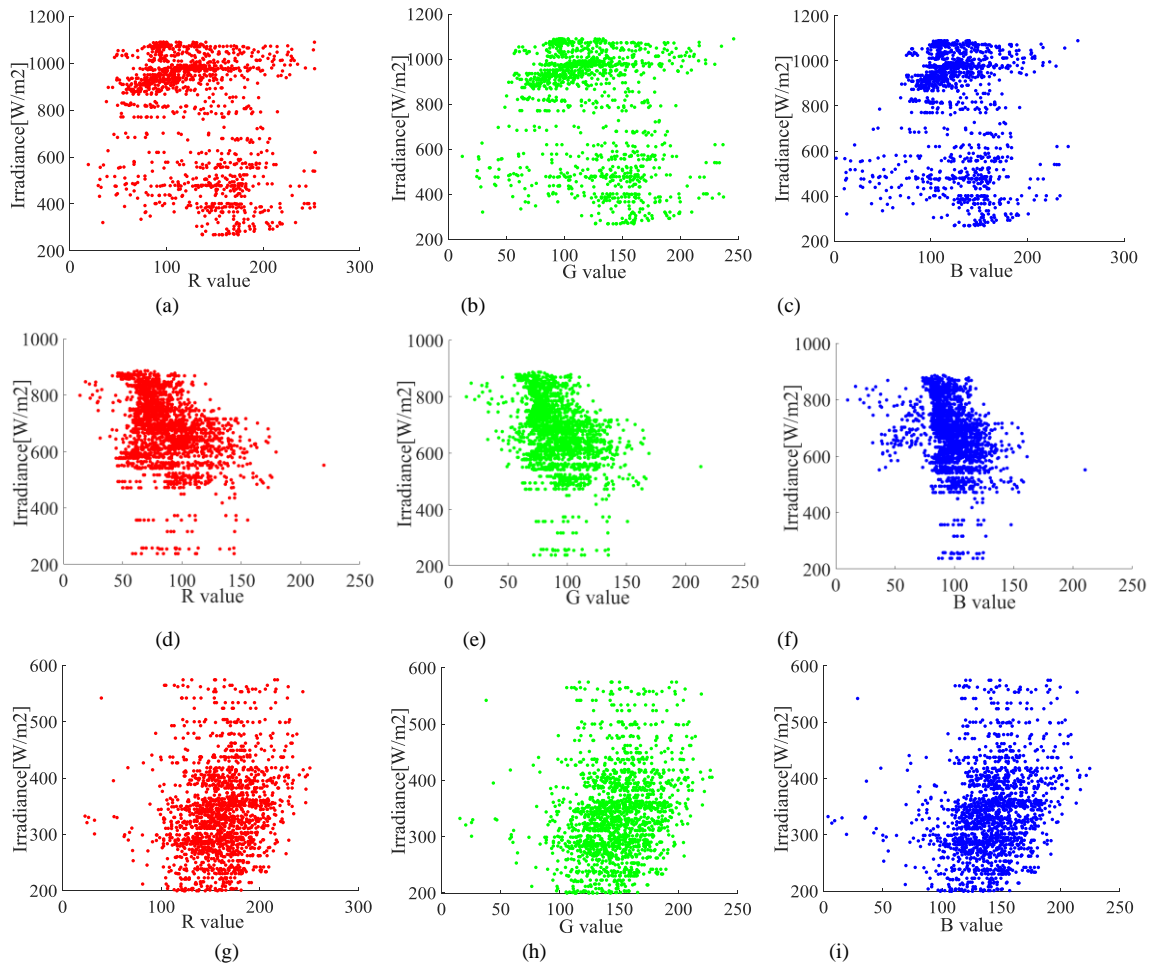
24



1 **Fig. 7.** Irradiance curves in 3 weather conditions.

2 When the sky is clear with no clouds, it is not hard to observe that the shape of irradiance curve is smooth and arched, which  
3 is only related to time lapses. For cloud-existing conditions, as we know, clouds are composed of water droplets, supercooled  
4 water droplets, and ice crystals. Thus, when cloud shape and thickness are both high enough that almost cover the whole sky  
5 area, plenty of these particles may result in sunlight reflection, so that significantly weaken the amount of irradiance reaching  
6 the earth's surface. As shown in Fig.7(a), when a cloud is passing by the sun, it may evoke irradiance fluctuations and account  
7 for a major value drop. While after going across the sun, irradiance value will rise up to a normal value as clear sky. As for thin  
8 cloud condition, the cloud-cover impact is not that severe compared with thick cloud, only slight fluctuation happens as  
9 demonstrated in Fig.7(b). In the case of thick clouds with high light-resistance property, the solar irradiance values will be  
10 attenuated to a great extent. Since the sunlight is still able to penetrate the cloud layer, the trend of irradiance curve is generally  
11 consistent with that of the clear sky, but the attenuation degree is more evident than the latter. The irradiance fluctuates rapidly  
12 due to the distribution and movement of the clouds next to the sun with various thickness extent and keeps at a quite low level  
13 during most of the time.

14 To provide theoretical support of proposed forecasting method, it is necessary to explore the relationship between RGB  
15 values of sky pixels and corresponding irradiance value. After cloud motion displacement calculation between two  
16 consecutive sky images, we can extract average RGB values of circular sky region which will cover the sun in the next few  
17 minutes, and corresponding irradiance at that moment as a group of samples. For each sky image, 10 groups of samples are  
18 chosen in total. We select 120 sky images in 2 h for each cloud condition, including blocky cloud, thin cloud, and thick cloud.  
19 Therefore, 1200 groups of samples can be generated. Then the relationship between R, G, B and irradiance can be explored  
20 respectively, which is presented in Fig.8.



21  
22  
23  
24  
25  
26  
27 **Fig. 8.** (a) Relationship between R value and irradiance in blocky cloud. (b) Relationship between G value and irradiance in blocky cloud. (c) Relationship  
28 between B value and irradiance in blocky cloud. (d) Relationship between R value and irradiance in thin cloud. (e) Relationship between G value and  
29 irradiance in thin cloud. (f) Relationship between B value and irradiance in thin cloud. (g) Relationship between R value and irradiance in thick cloud. (h)  
30 Relationship between G value and irradiance in thick cloud. (i) Relationship between B value and irradiance in thick cloud.






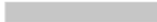
Colors	RGB	Colors	RGB
	(0, 0, 225)		(100, 100, 100)
	(51, 85, 221)		(150, 150, 150)
	(102, 170, 221)		(180, 180, 180)

Fig. 9. Several colors in sky image with corresponding RGB values.

It is shown in Fig.8 that in the case of blocky cloud, most spots gather at the top left and bottom right, which indicates that irradiance values keep at a low level when RGB values are around the center (150,150,150)(a gray color shown in Fig.9), while irradiance much higher when RGB values are around (80,100,130), which represents part of blue sky region mixed in. For different kinds of blue colors, the values in R and G channels are both less than blue one, resulting in difference among RGB values of center points. In the situation of thin cloud which depicted in Fig.8(d)-Fig.8(f), the distributions of RGB spots are both downward sloping, representing that pixel points which around (120,120,120) are thin cloud coverage, while the points around (60,80,100) are in blue sky environment. On the consideration of blue-white mixture, there may be a deviation between derived RGB values and real pixel RGB values. As for thick cloud condition described in Fig.8(g)-Fig.8(i), the distribution trends of RGB are towards upper right. That means when the RGB values are around (170,170,170), the amount of irradiance which can penetrate clouds is less, thus representing a thick cloud circumstance. Therefore, we can draw a conclusion that irradiance is subject to pixel's RGB values, which theoretically prove that the proposed method based on sky image-irradiance mapping model is practical.

### 2.6 Minutely irradiance forecasting method based on real-time sky image-irradiance mapping model

Except for RGB values, pixel location information is another essential factor affecting irradiance value. As for same cloud, various distances from the cloud to the sun center will cause differences on cloud RGB values. The nearer to the sun, the cloud is brighter, even though there is no change on the cloud thickness. Therefore, during the mapping model establishment, inputs consist of RGB values and distance information, with irradiance output are selected to train the mapping model. Then a sky image-irradiance mapping is derived. After updating the mapping model to adapt to the current cloud conditions with new data in real time, minutely irradiance forecasting can be achieved on this basis.

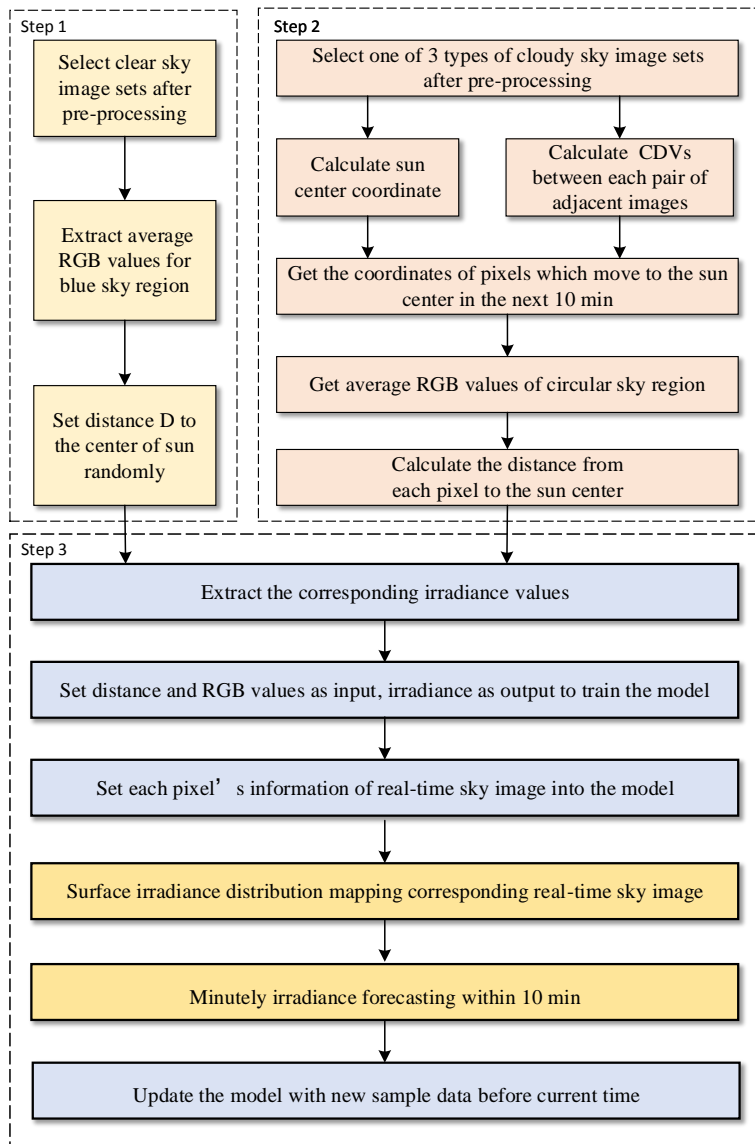


Fig. 10. The process of minutely irradiance forecasting based on real-time sky image-irradiance mapping model.

The main technology route of minute-level irradiance forecasting based on real-time sky image-irradiance mapping model is described as follows:

- 1) Extract several clear sky image sets and one of 3 types of cloudy sky image sets.
- 2) Pre-process each image sets with background elimination and distortion rectification techniques.
- 3) Calculate cloud motion displacement vectors between each two consecutive cloudy sky images.
- 4) Calculate the coordinates of the sun center in each sky image.
- 5) Calculate the coordinates of pixels that moving to the sun center in the next 10 min from each sky image.
- 6) Set  $R$  as radius with the center point calculated in step 5), extract average RGB values of pixels located in this circular region; as for clear sky image sets, extract average RGB values of pixels in the whole blue sky area.
- 7) Calculate the distance  $D$  between the sun center and the coordinates calculated in step 5); for clear sky image sets, distance  $D$  is randomly set from 10 to 200.
- 8) Extract corresponding irradiance values.
- 9) Set RGB values and distance  $D$  as 4-dimensional input, irradiance value as 1-dimensional output to train mapping model.
- 10) Set each pixel's information of real-time sky image into the model.

- 11) The surface irradiance distribution mapping figure corresponding to real-time sky image is generated.
- 12) Based on cloud motion displacement forecast by using linear extrapolation, pixel's information in 10 min are acquired from the mapping graph in step 11). Then after model training with pixel's information, minutely irradiance forecasting can be achieved within 10 min.
- 13) Update the model with new sample data before the current time. Repeat all steps from step 1).

The flow diagram is illustrated in Fig.10.

### III. CASE STUDY

#### 3.1 Data

Sky image sets and historical irradiance data in this paper are acquired from Wasco power station in Earth System Research Laboratory (ESRL) on National Oceanic and Atmospheric Administration (NOAA). According to the weather type classification method depicted in Section 2.4, we select a 20-day dataset in each cloud condition, including blocky cloud, thin cloud, thick cloud, and clear sky. Since the time resolution of the image is 30 s and the irradiance data are logged at a sampling rate of 1 min, we select average resolution as 1 min for both datasets. Considering sky imager is incapable of conducting image collection at night, sky images and irradiance are selected from 7:00 to 17:00 for model training. In order to provide more sky information, processed images are also required for invalid background elimination, with a resolution of 640×480.

#### 3.2 Simulation process

In this part, key process of model establishment is analyzed and introduced in detail. We follow the methodologies mentioned above to establish sky-image mapping model in different cloud conditions: blocky cloud, thin cloud and thick cloud individually. In each training model, 20-day clear sky sets and 10-day image sets in forecasted cloud condition are selected as training data. The rest 10-day image sets in the forecasted cloud condition are used to test the performance of irradiance forecasting methods.

After image background elimination and distortion rectification, more accurate cloud motion displacement results can be obtained from each two consecutive sky images by improved FPC. According to the theory of accumulative principle, the circular regions with radius  $R$  which will cover the sun in the next 10 min can be derived based on calculated CDVs. In this paper, we raise an assumption with high credibility that the irradiance value is mainly related with the circular region which cover the sun. In consideration of various distance between the sun and the same coverage region in a series of consecutive sky images, average RGB values of the same circular region will evoke a great variation due to halo phenomenon. Therefore, distance  $D$  between circular region and the sun center is necessary to be taken into account as one of model input.

For instance, if we are willing to predict irradiance from 16:01 to 16:10 on May 18, 2016 by using this mapping model, sample set are selected before 16:00, May 18, 2016. As sky image-irradiance mapping model technical route described in Section 2.6, circular regions in each image which will cover the sun in next 10 min with corresponding irradiance values enable to be acquired based on CDV calculation. However, there is no guarantee that 10 groups of samples can be extracted from each sky image. Some reasons may cause this phenomenon :1) part of sky area is sheltered by shadow-band and support arms; 2) CDVs are inconsistent for different cloud layers; 3) when the sun position is close to the edge of fish glasses, not all extracted pixel coordinates are located in acceptable sky region part. Generally, the pixels often fall in the invalid background area, making these groups of information completely unusable.

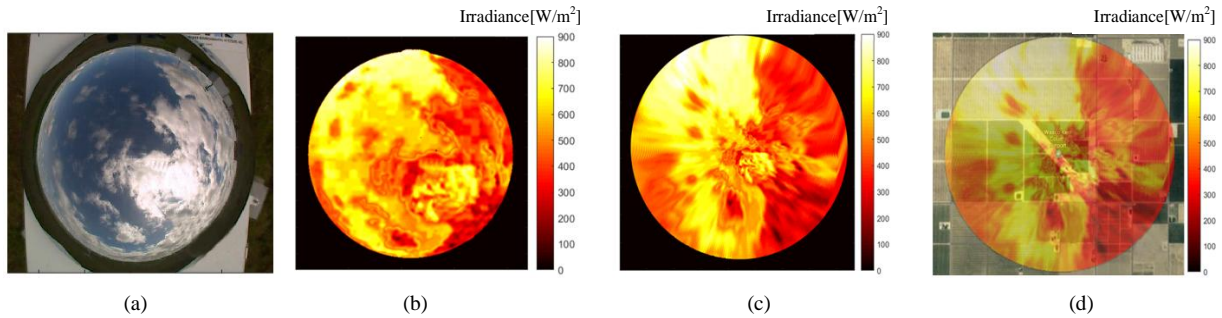
Then we can extract average RGB values of coverage circular regions and distance  $D$  as input, while corresponding irradiance values as output to train the forecasting model. After that, import each pixel's information of real-time sky image at 16:00 into this model, the output image can be seemed as irradiance mapping figure at current time. Based on cloud-base height, the mapping radius can be derived, then a ground surface irradiance mapping figure is available. To verify the accuracy of this mapping figure, we utilize the ground surface irradiance mapping figure and CDVs for each minute in 10-min timescale before real-time moment, in order to extract the corresponding input in every minute. After putting input into established model, forecasted values of previous irradiance can be derived. If the error between the predicted and actual irradiance is less than a pre-defined threshold, then the ground surface irradiance mapping result can be seemed close to actual situation. To achieve minutely irradiance forecasting up to 10 min ahead horizon, circular regions can be predicted and extracted as future coverage region based on linear extrapolation CDVs calculation. Then each pixel's information is able to be put into the training model, thus forecasting irradiance output can be acquired.

Here we apply multiple approaches including two benchmarks and our proposed method with different training models to

1 test both of these methods' performance of irradiance forecasting in 3 different weather cases. 4 forecasting methods are  
2 listed as follows.

- 3 1) Proposed method with pixel information input by using BPNN training model.
- 4 2) Proposed method with pixel information input by using SVM training model.
- 5 3) Irradiance forecasting by autoregressive integrated moving average model (ARIMA).
- 6 4) Conventional prediction model with input including temperature, humidity and irradiance in 3 min before the  
7 current moment by using BPNN training model.

### 8 3.3 Results and discussion



9  
10  
11 **Fig. 11.** (a) Raw sky image. (b) Irradiance distribution mapping corresponding to raw sky image. (c) Irradiance distribution mapping corresponding to sky  
12 image after distortion rectification. (d) Actual surface irradiance distribution mapping.

13 In this paper, BPNN and SVM are adopted for model training, so as to present sky image-irradiance mapping results. The  
14 training set and validation set account for 80% and 20% of the sample set respectively. According to the experience, we select  
15 two hidden layers in BPNN, the first layer is set as 6, and the second layer is set as 5. The predicted results corresponding sky  
16 image in Fig.11(a) are depicted as Fig.11(b). To omit the pixels in invalid background area, we set gray value of background  
17 area as zero. Since the regions corresponding to different pixel points are identified by processed images, the edge information  
18 of the sky image is deleted to retain most of the real sky region information, resulting in the effective sky region of the  
19 irradiance mapping image is smaller than the ones of original sky image. As for Fig.11(c), which processed with image  
20 distortion rectification technique, it represents the real mapping condition corresponding to Fig.11(a). According to the fact  
21 that the cloud base is approximately at 3500 meters high, the radius of surface irradiance distribution mapping is calculated as  
22 2000 meters. Combined with PV station map, the actual situation of surface irradiance distribution mapping can be showed as  
23 Fig.11(d). With manual observation, it is easy to observe that the irradiance values of blue sky pixels are generally high, while  
24 those of white clouds are quite low, which are consistent with the real situation.

25 In order to verify the accuracy of the surface irradiance mapping model presented in this paper, we apply a simple method to  
26 testify. First, calculate the CDVs between 10 consecutive pairs of sky images before current time, thus the information of the  
27 sky region center which would cover the sun over the past 10 min can be derived. After utilizing established forecasting model,  
28 corresponding predicted irradiance in 10 min ago can be obtained in minute level. If the absolute value of the error between  
29 forecasting and actual irradiance values is less than 80, then we assume that the forecasting value can be accepted. Therefore,  
30 when most of the ten points accord with this condition, the results of this mapping model can be regarded as credible.

31 Table 3 demonstrates the accuracy and reliability of the proposed surface irradiance distribution mapping model in 3  
32 different weather conditions based on several evaluation indexes. There are at least 8 points according with the validation  
33 method mentioned above, resulting in accuracy fluctuation around 80%. In other words, that means the accuracy of surface  
34 irradiance distribution mapping can be up to 80%. After determining the usability of mapping figure, minutely irradiance  
35 forecasting in next 10 min can be achieved. By taking advantage of linear extrapolation to forecast CDVs, the sky region part  
36 which will cover the sun can be gained, thus achieve input information extraction. Then the forecasting irradiance outputs can  
37 be acquired by using forecasting model. Fig.12 shows the actual and forecasting irradiance during next 10 min in 3 types of  
38 weather conditions.

39 **Table 3** Evaluation indexes to verify the credibility of mapping model in 3 weather conditions.



Case	Number of accepted points	Accuracy (%)	RMSE (W/m <sup>2</sup> )	MAPE (%)
Blocking cloud	8	80	71.24	13.09
Thin cloud	9	90	55.26	11.86
Thick cloud	9	90	45.82	9.44

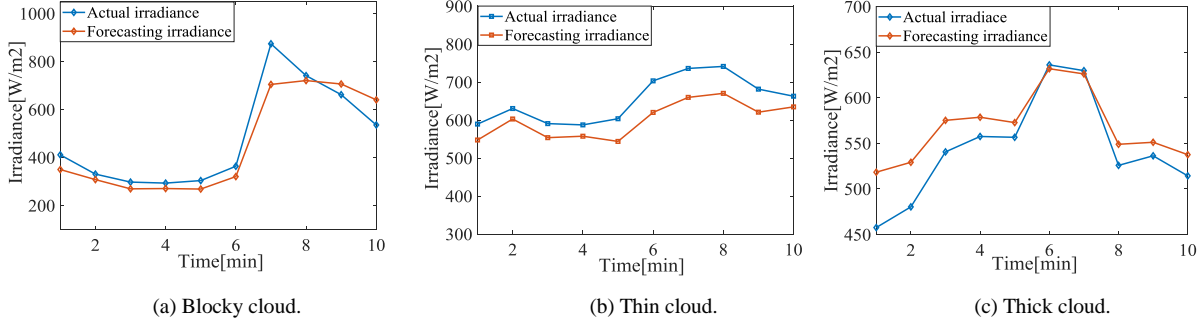


Fig. 12. Forecasting and real irradiance values in next 10 min for 3 cloud cases.

In order to observe the performance of proposed method directly and conveniently, rolling prediction is applied to forecast future irradiance values in 2 hours. The predicted values in the 10<sup>th</sup> min are extracted. The results in 3 weather types are depicted in Fig.13.

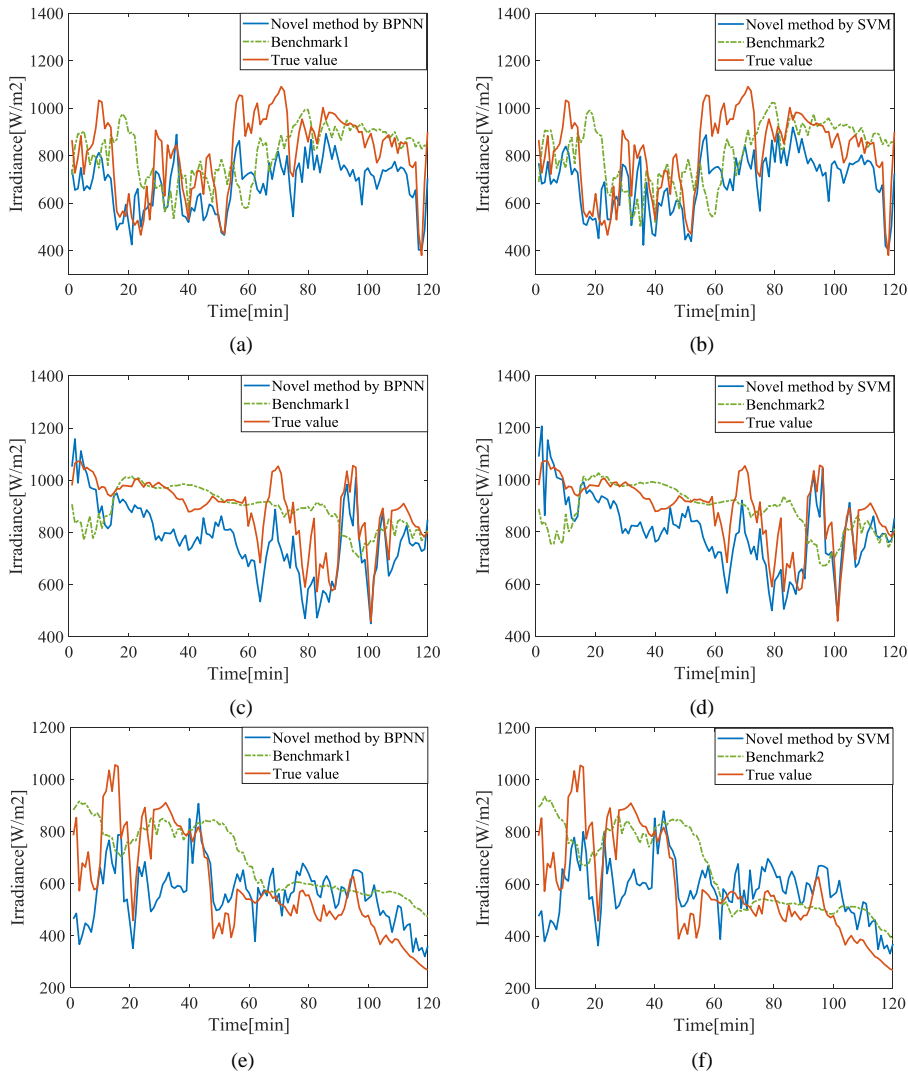
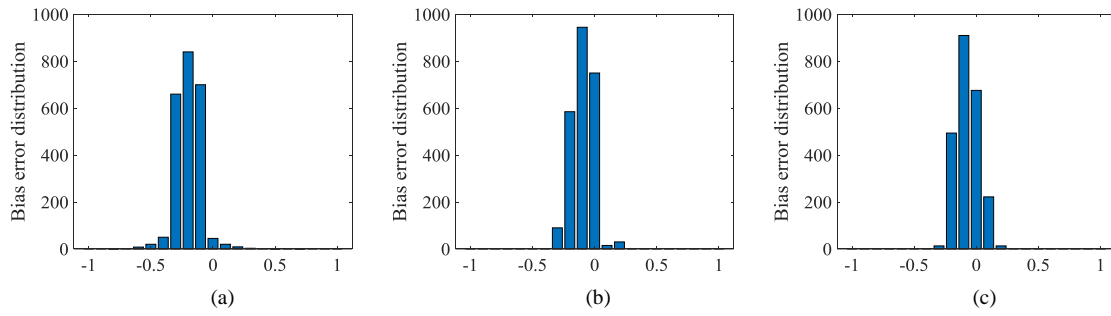


Fig.13. Minutely irradiance forecasting curves within 2 h in 3 weather types. (a) Forecasts in blocky cloud condition by using BPNN and benchmark 1. (b) Forecasts in blocky cloud condition by using SVM and benchmark 2. (c) Forecasts in thin cloud condition by using BPNN and benchmark 1 (d) Forecasts in

1 thin cloud condition by using SVM and benchmark 2 (e) Forecasts in thick cloud condition by using BPNN and benchmark 1 (f) Forecasts in thick cloud  
 2 condition by using SVM and benchmark 2.



3  
4  
5 **Fig. 14.** Distribution forecasting error in 3 weather conditions: (a) blocky cloud; (b) thin cloud; (c) thick cloud.

6 **Table 4** Evaluation indexes in 3 weather conditions by using 4 different methods.

Methods	Evaluation Indexes	Weather Conditions		
		Blocky cloud	Thin cloud	Thick cloud
BPNN	MAPE(%)	23.81	<b>20.44</b>	<b>18.82</b>
	RMSE(W/m <sup>2</sup> )	98.17	<b>132.15</b>	<b>120.78</b>
	MBE(%)	-1.28	<b>-1.06</b>	-1.02
SVM	MAPE(%)	<b>22.66</b>	20.88	19.58
	RMSE(W/m <sup>2</sup> )	<b>92.72</b>	134.82	120.85
	MBE(%)	<b>-1.26</b>	-1.08	<b>-0.98</b>
Benchmark1	MAPE(%)	34.61	28.72	27.83
	RMSE(W/m <sup>2</sup> )	184.43	162.63	130.61
	MBE(%)	2.62	-2.26	-1.66
Benchmark2	MAPE(%)	30.58	24.32	22.34
	RMSE(W/m <sup>2</sup> )	160.24	142.74	127.25
	MBE(%)	2.32	-2.05	-1.42

7  
8 It is shown in Fig.13 that the irradiance values from 14:00 to 16:00 are predicted in 3 weather types. Under the conditions of  
 9 all cloudy weather, predicted output by BPNN and SVM considerably show the relatively correct irradiance trend than other  
 10 benchmarks. Compared with statistical times-series method as benchmark 1, the proposed method based on cloud information  
 11 characteristic extraction is capable of reducing time lag effect to a certain extent. As for benchmark 2, only historical  
 12 irradiance input unable to provide useful information to achieve high-accuracy forecasting excluding strong-correlational and  
 13 instructional factors to future irradiance. To evaluate the performance on over-forecasting and under-forecasting, forecasting  
 14 bias is provided by using the mean bias error (MBE) index. In Fig.14, the histograms of the occurrences of minutely values of  
 15 MBE are presented. For the sake of the testing sample size, real irradiance value in each moment is considered as the  
 16 denominator in the formula of MBE, not the maximum irradiance value during a period of time, which results in higher MBE  
 17 values compared with the ones shown in Table 4. To evaluate various forecasting methods comprehensively, forecasting  
 18 results are set out by different statistical parameters, including mean absolute percentage error (MAPE), root-mean-square  
 19 error (RMSE), and MBE shown in Table 4. For each weather condition, 10 days are used for testing. From this table, it is  
 20 easy to observe that the forecast accuracy of proposed method with BPNN and SVM model is better than other benchmarks.  
 21 Most of the best forecasting results in each condition are generated by using BPNN with sky pixel's information model input.  
 22 For the sake of irradiance mutability in blocky cloud condition, the evaluation indexes are generally higher than other two  
 23 weather conditions. The average measures come up to 22.66%, 92.72, -1.26% for MAPE, RMSE, MBE respectively, which  
 24 can be considered as the most difficult condition to be predicted. In the third cloud condition, due to the cloud characteristic  
 25 with high thickness and massive block, the sun is almost covered during a long period. The daily irradiance curve maintains at  
 26 a low value with a small fluctuation range, while the prediction results are close to real fluctuation compared with the results  
 27 generated by the other two benchmarks. To sum up, the accuracy of proposed method by using BPNN and SVM models is  
 28 shown to be adequate for minutely irradiance forecasting which presents a better performance than compared methods in both  
 29 3 weather conditions.

30 The results analyzed above represent an ideal accuracy of the novel method on the ultra-short-term irradiance forecasting  
 31 with time horizons of 10 min. However, many factors will cause accuracy reduction during forecasting process. When



1 calculating the displacement vector of the cloud motion in a set of sky images, the real cloud motion situation is extraordinarily  
2 complex and challenging to be described by a mathematical model. What's more, cloud generation, elimination, deformation,  
3 various motion directions and velocities in different layers will definitely cause high noise to displacement vector  
4 calculation, making the final result probably inconsistent with the actual situation. Besides, the distortion effect caused by the  
5 spherical mirror of TSI also brings errors to the judgment of real cloud motion. Despite TSI is installed with image processed  
6 system to process original images, distortion problem is still existing after related image processing, especially for the edge  
7 part of sky image. The training model is also unable to identify the halo formed by the sun, which is easily identified as cloud  
8 pixel. Besides, in this paper, RGB values of the pixel point are averaged by the ones in a circular region. In actual process, it  
9 will cause a mixture of blue sky and white cloud pixels, which leads to inaccuracy on irradiance forecasting.

#### 10 IV. CONCLUSION

11 This paper proposed a minutely solar irradiance forecasting method based on real-time surface irradiance mapping model.  
12 We first explored the mapping relationship between cloud pixels' information and irradiance, then built a real-time sky  
13 image-irradiance mapping model on this basis. Considering the sky information deficiency and image distortion phenomenon  
14 during the ground-based sky imaging systems shooting process, we apply background elimination and distortion rectification  
15 to restore actual mapping situation. During mapping model establishment, RGB values and location information of circular  
16 sky region which will cover the sun in the next 10 min are extracted as model input, while the corresponding irradiance is  
17 selected as the output. On the basis of this well-established model, surface irradiance mapping figure for real-time sky image  
18 can be obtained. After cloud motion displacement forecast by linear extrapolation, minute-level irradiance forecasting for time  
19 horizon varying from 1 min to 10 min can be achieved. Due to the mapping relationship between sky image and irradiance is  
20 changing dynamically, the mapping model is set to be trained and updated according to real-time data continuously.

21 The simulation results show that the proposed method can achieve an exact mapping model from real-time sky image to  
22 surface irradiance distribution. After completion of mapping model establishment, forecasting method with pixel's  
23 information input based BPNN and SVM can better track the fast fluctuation of irradiance in various cloud conditions, thus  
24 deliver more accurate forecasting results compared with other two benchmarks. Based on the proposed real-time surface  
25 irradiance mapping model, we can achieve a more detailed irradiance distribution map around the local PV power station, so as  
26 to help realize a minutely forecasting of rapid fluctuations in PV power output.

#### 27 ACKNOWLEDGEMENT

28 This work was supported by the National Key R&D Program of China (Technology and application of wind power /  
29 photovoltaic power prediction for promoting renewable energy consumption, 2018YFB0904200) and eponymous  
30 Complement S&T Program of State Grid Corporation of China (SGLNDKOOKJJS1800266).

#### 31 REFERENCES

- 32 [1] Wang F, Zhang Z, Liu C, Yu Y, Pang S, Duić N, et al. Generative adversarial networks and convolutional neural networks based weather classification  
33 model for day ahead short-term photovoltaic power forecasting. *Energy Convers Manag* 2019;181:443–62.  
34 <https://doi.org/10.1016/j.enconman.2018.11.074>.
- 35 [2] Li K, Mu Q, Wang F, Gao Y, et al. A business model incorporating harmonic control as a value-added service for utility-owned electricity retailers. *IEEE*  
36 *Trans Ind Appl* 2019;55:4441–50. <https://doi.org/10.1109/TIA.2019.2922927>.
- 37 [3] Cui M, Zhang J, Feng C, Florita AR, Sun Y. Characterizing and analyzing ramping events in wind power, solar power, load, and netload. *Renew Energy*  
38 2017;111:227-224. <https://doi.org/10.1016/j.renene.2017.04.005>.
- 39 [4] Wang F, Zhen Z, Wang B, Mi Z. Comparative study on KNN and SVM based weather classification models for day ahead short term solar PV power  
40 forecasting. *Appl Sci* 2017;8:28. <https://doi.org/10.3390/app8010028>.
- 41 [5] Sivaram PM, Mande AB, Premalatha M, Arunagiri A. Investigation on a building-integrated passive solar energy technology for air ventilation , clean  
42 water and power. *Energy Convers Manag* 2020;211:112739. <https://doi.org/10.1016/j.enconman.2020.112739>.
- 43 [6] Alam MJE, Muttaqi KM, Sutanto D. A novel approach for ramp-rate control of solar PV using energy storage to mitigate output fluctuations caused by  
44 cloud passing. *IEEE Trans Energy Convers* 2014;29(2):507–18. <https://doi.org/10.1109/tec.2014.2304951>.
- 45 [7] Zhen Z, Pang S, Wang F, Li K, Li Z, Ren H, et al. Pattern classification and PSO optimal weights based sky images cloud motion speed calculation method  
46 for solar PV power forecasting. *IEEE Trans Ind Appl* 2019;55:3331–42. <https://doi.org/10.1109/TIA.2019.2904927>.
- 47 [8] Quesada-ruiz S, Chu Y, Tovar-pescador J, Pedro HTC, Coimbra CFM. Cloud-tracking methodology for intra-hour DNI forecasting. *Sol Energy*  
48 2014;102:267–75. <https://doi.org/10.1016/j.solener.2014.01.030>.
- 49 [9] Li K, Wang F, Mi Z, Fotuhi-firuzabad M, Dui N, Wang T. Capacity and output power estimation approach of individual behind-the- meter distributed

- 1 photovoltaic system for demand response baseline estimation. *Appl Energy* 2019;253:113595. <https://doi.org/10.1016/j.apenergy.2019.113595>.
- 2 [10] Shivashankar S, Mekhilef S, Mokhlis H, Karimi M. Mitigating methods of power fluctuation of photovoltaic (PV) sources – A review. *Renew Sustain*  
3 *Energy Rev* 2016;59:1170–84. <https://doi.org/10.1016/j.rser.2016.01.059>.
- 4 [11] Amjady N, Fallahi F. Determination of frequency stability border of power system to set the thresholds of under frequency load shedding relays. *Energy*  
5 *Convers Manag* 2010;51:1864–72. <https://doi.org/10.1016/j.enconman.2010.02.016>.
- 6 [12] Ghennam T, Aliouane K, Akel F, Francois B, Berkouk EM. Advanced control system of DFIG based wind generators for reactive power production and  
7 integration in a wind farm dispatching. *Energy Convers Manag* 2015;105:240–50. <https://doi.org/10.1016/j.enconman.2015.07.058>.
- 8 [13] Perkins G. Techno-economic comparison of the levelised cost of electricity generation from solar PV and battery storage with solar PV and combustion of  
9 bio-crude using fast pyrolysis of biomass. *Energy Convers Manag* 2018;171:1573–88. <https://doi.org/10.1016/j.enconman.2018.06.090>.
- 10 [14] Wang F, Xu H, Xu T, Li K, Shafie-khah M, Catalão JPS. The values of market-based demand response on improving power system reliability under  
11 extreme circumstances. *Appl Energy* 2017;193:220–31. <https://doi.org/10.1016/j.apenergy.2017.01.103>.
- 12 [15] Li K, Liu L, Wang F, Wang T, Dui N, Sha M, et al. Impact factors analysis on the probability characterized effects of time of use demand response tariffs  
13 using association rule mining method. *Energy Convers Manag* 2019;197:111891. <https://doi.org/10.1016/j.enconman.2019.111891>.
- 14 [16] Wang F, Mi Z, Su S, Zhao H. Short-term solar irradiance forecasting model based on artificial neural network using statistical feature parameters. *Energies*  
15 2012;5:1355–70. <https://doi.org/10.3390/en5051355>.
- 16 [17] Yuan X, Ji B, Zhang S, Tian H, Chen Z. An improved artificial physical optimization algorithm for dynamic dispatch of generators with valve-point effects  
17 and wind power. *Energy Convers Manag* 2014;82:92–105. <https://doi.org/10.1016/j.enconman.2014.03.009>.
- 18 [18] Mohammed A, Pasupuleti J, Khatib T. Simplified performance models of photovoltaic/diesel generator/battery system considering typical control  
19 strategies. *Energy Convers Manag* 2015;99:313–25. <https://doi.org/10.1016/j.enconman.2015.04.024>.
- 20 [19] Wang F, Li K, Liu C, Mi Z, et al. Synchronous pattern matching principle-based residential demand response baseline estimation : mechanism analysis and  
21 approach description. *IEEE T Smart Grid* 2018;9:6972–85. <https://doi.org/10.1109/TSG.2018.2824842>.
- 22 [20] Wang F, Zhen Z, Mi Z, Sun H, Su S, Yang G. Solar irradiance feature extraction and support vector machines based weather status pattern recognition  
23 model for short-term photovoltaic power forecasting. *Energy Build* 2015;86:427–38. [doi:10.1016/j.enbuild.2014.10.002](https://doi.org/10.1016/j.enbuild.2014.10.002).
- 24 [21] Wang F, Yu Y, Zhang Z, Li J, Li K. Wavelet decomposition and convolutional LSTM networks based improved deep learning model for solar irradiance  
25 forecasting. *Appl Sci* 2018;8:1286. <https://doi.org/10.3390/app8081286>.
- 26 [22] Esmael M, Hosseinnzhad V. A peak-load-reduction-based procedure to manage distribution network expansion by applying process-oriented costing of  
27 incoming components. *Energy* 2019;186:115852. <https://doi.org/10.1016/j.energy.2019.115852>.
- 28 [23] Chen C, Duan S, Cai T, Liu B. Online 24-h solar power forecasting based on weather type classification using artificial neural network. *Sol Energy*  
29 2011;85:2856–70. <https://doi.org/10.1016/j.solener.2011.08.027>.
- 30 [24] Malvoni M, Hatziargyriou N. One-day ahead PV power forecasts using 3D Wavelet Decomposition. In: 2019 International Conference on Smart Energy  
31 Systems and Technologies (SEST). Porto, Portugal; Sep 2019. p. 1–6.
- 32 [25] Wang F, Xuan Z, Zhen Z, Li K, Wang T, Shi M. A day-ahead PV power forecasting method based on LSTM-RNN model and time correlation modi fi  
33 cation under partial daily pattern prediction framework. *Energy Convers Manag* 2020;212:112766. <https://doi.org/10.1016/j.enconman.2020.112766>.
- 34 [26] Zhang C, Du Y, Chen X, et al. Cloud motion tracking system using low-cost sky imager for PV power ramp-rate control. In: 2018 IEEE International  
35 Conference on Industrial Electronics for Sustainable Energy Systems (IESES). Hamilton, New Zealand; Jan 2018. p.  
36 493-498. <https://doi.org/10.1109/ieses.2018.8349927>.
- 37 [27] Li M, Chu Y, Pedro HTC, Coimbra CFM. Quantitative evaluation of the impact of cloud transmittance and cloud velocity on the accuracy of short-term  
38 DNI forecasts. *Renew Energ* 2016;86:1362-71. <http://dx.doi.org/10.1016/j.renene.2015.09.058>.
- 39 [28] Kumar M, Majumder I, Nayak N. Solar photovoltaic power forecasting using optimized modified extreme learning machine technique. *Eng Sci Technol*  
40 *an Int J* 2018;21:428-438. <https://doi.org/10.1016/j.jestch.2018.04.013>.
- 41 [29] Liu J, Fang W, Zhang X, Yang C. An improved photovoltaic power forecasting model with the assistance of aerosol index data. *IEEE T Sustain Energy*  
42 2015;6:434-442. <https://doi.org/10.1109/TSTE.2014.2381224>.
- 43 [30] Ramsami P, Oree V. A hybrid method for forecasting the energy output of photovoltaic systems. *Energy Convers Manag* 2015;95:406–13.  
44 <https://doi.org/10.1016/j.enconman.2015.02.052>.
- 45 [31] Lorenz E, Hurka J, Heinemann D, Beyer HG. Irradiance forecasting for the power prediction of grid-connected photovoltaic systems. *IEEE J-STARS*  
46 2009;2:2–10. <https://doi.org/10.1109/jstars.2009.2020300>.
- 47 [32] Mathiesen P, Kleissl J. Evaluation of numerical weather prediction for intra-day solar forecasting in the continental United States. *Sol Energy*

- 1 2011;85:967–77. <https://doi:10.1016/j.solener.2011.02.013>.
- 2 [33] Marquez R, Coimbra CFM. Forecasting of global and direct solar irradiance using stochastic learning methods, ground experiments and the NWS database.  
3 Sol Energy 2011;85:746–56. <https://doi:10.1016/j.solener.2011.01.007>.
- 4 [34] Hoff TE, Perez R. Quantifying PV power output variability. Sol Energy 2010;84:1782–93. <https://doi:10.1016/j.solener.2010.07.003>.
- 5 [35] Zhen Z, Xuan Z, Wang F, Sun R, Dui N, Jin T. Image phase shift invariance based multi-transform-fusion method for cloud motion displacement  
6 calculation using sky images. Energy Convers Manag 2019;197:111853. <https://doi:10.1016/j.enconman.2019.111853>.
- 7 [36] Tzoumanikas P, Nikitidou E, Bais AF, Kazantzidis A. The effect of clouds on surface solar irradiance, based on data from an all-sky imaging system.  
8 Renew Energy 2016;95:314–22. <https://doi:10.1016/j.renene.2016.04.026>.
- 9 [37] Yabuki M, Shiobara M, Nishinaka K, Kuji M. Development of a cloud detection method from whole-sky color images. Polar Sci 2014;8:315–26.  
10 <https://doi:10.1016/j.polar.2014.07.004>.
- 11 [38] Marquez R, Coimbra CFM. Proposed metric for evaluation of solar forecasting models. J Sol Energ-T Asme 2016;135:011016.  
12 <https://doi.org/10.1115/1.4007496>.
- 13 [39] Wai C, Urquhart B, Lave M, Dominguez A, Kleissl J, Shields J, et al. Intra-hour forecasting with a total sky imager at the UC San Diego solar energy  
14 testbed. Sol Energy 2011;85:2881–93. <https://doi:10.1016/j.solener.2011.08.025>.
- 15 [40] Ghonima MS, Urquhart B, Chow CW, Shields JE, Cazorla A, Kleissl J. A method for cloud detection and opacity classification based on ground based sky  
16 imagery. Atmos Meas Tech 2012;5:2881–92. <https://doi.org/10.5194/amt-5-2881-2012>.
- 17 [41] Rana M, Koprinska I, Agelidis VG. Univariate and multivariate methods for very short-term solar photovoltaic power forecasting. Energy Convers Manag  
18 2016;121:380–90. <https://doi:10.1016/j.enconman.2016.05.025>.
- 19 [42] Alonso-montesinos J, Batlles FJ, Portillo C. Solar irradiance forecasting at one-minute intervals for different sky conditions using sky camera images.  
20 Energy Convers Manag 2015;105:1166–77. <https://doi:10.1016/j.enconman.2015.09.001>.
- 21 [43] Peng Z, Yu D, Huang D, Heiser J, Kalb P. A hybrid approach to estimate the complex motions of clouds in sky images. Sol Energy 2016;138:10–25.  
22 <https://doi:10.1016/j.solener.2016.09.002>.
- 23 [44] Wai C, Belongie S, Kleissl J. Cloud motion and stability estimation for intra-hour solar forecasting. Sol Energy 2015;115:645–55.  
24 <https://doi:10.1016/j.solener.2015.03.030>.
- 25 [45] Wang F, Zhen Z, Liu C, Mi Z, Hodge B, Sha M, et al. Image phase shift invariance based cloud motion displacement vector calculation method for  
26 ultra-short-term solar PV power forecasting. Energy Convers Manag 2018;157:123–35. <https://doi:10.1016/j.enconman.2017.11.080>.
- 27 [46] Zhen Z, Liu J, Zhang Z, et al. Deep Learning Based Surface Irradiance Mapping Model for Solar PV Power Forecasting Using Sky Image. IEEE Trans Ind  
28 Appl 2020; Early Access. <http://doi:10.1109/TIA.2020.2984617>.
- 29 [47] Li K, Cao X, Ge X, et al. Meta-Heuristic Optimization Based Two-stage Residential Load Pattern Clustering Approach Considering Intra-cluster  
30 Compactness and Inter-cluster Separation. IEEE Trans Ind Appl 2020; Early Access. <http://doi:10.1109/TIA.2020.2984410>.
- 31 [48] Yang S, Li K, et al. Time–Frequency Feature Combination Based Household Characteristic Identification Approach Using Smart Meter Data. IEEE Trans  
32 Ind Appl 2020; 56: 2251–2262. <http://doi:10.1109/TIA.2020.2981916>.
- 33 [49] Wang F, et al. Association rule mining based quantitative analysis approach of household characteristics impacts on residential electricity consumption  
34 patterns. Energy Convers. Manag 2018; 171: 839–854. <http://doi:10.1016/j.enconman.2018.06.017>.
- 35 [50] Wang F, Xiang B, et al. Smart Households’ Aggregated Capacity Forecasting for Load Aggregators under Incentive-based Demand Response Programs.  
36 IEEE Trans Ind Appl 2020; 56: 1086–1097. <http://doi:10.1109/TIA.2020.2966426>.
- 37 [51] Lu X, Yu X, Lai J, Wang Y, Guerrero JM. A Novel Distributed Secondary Coordination Control Approach for Islanded Microgrids,” IEEE Trans. Smart  
38 Grid 2018; 9: 2726–2740. <http://doi:10.1109/TSG.2016.2618120>.
- 39 [52] Lu X, Yu X, Lai J, Guerrero JM, Zhou H. Distributed Secondary Voltage and Frequency Control for Islanded Microgrids With Uncertain Communication  
40 Links. IEEE Trans. Ind. Inform 2017; 13: 448–460. <http://doi:10.1109/TII.2016.2603844>.
- 41 [53] J. Lai, Zhou H, Lu X, Yu X, Wu W. Droop-Based Distributed Cooperative Control for Microgrids With Time-Varying Delays. IEEE Trans. Smart Grid  
42 2016; 7: 1775–1789. <http://doi:10.1109/TSG.2016.2557813>.
- 43 [54] Magdy G, Mohamed E.A, Shabib G. et al. Microgrid dynamic security considering high penetration of renewable energy. Prot Control Mod Power Syst  
44 2018; 3: 23. <https://doi.org/10.1186/s41601-018-0093-1>.
- 45 [55] Zhang D, Li J, Hui D. Coordinated control for voltage regulation of distribution network voltage regulation by distributed energy storage systems. Prot.  
46 Control Mod. Power Syst 2018; 3:35-42. <https://doi.org/10.1186/s41601-018-0077-1>.
- 47 [56] Chen Q. et al. Dynamic price vector formation model-based automatic demand response strategy for PV-assisted EV charging stations. IEEE Trans. Smart

